nature COMMUNICATIONS

ARTICLE

https://doi.org/10.1038/s41467-022-28924-2 OPEN

Check for updates

Quantum-enabled operation of a microwave-optical interface

Rishabh Sahu[1]✉, William Hease[1], Alfredo Rueda[1], Georg Arnold[1], Liu Qiu[1] & Johannes M. Fink[1]✉

Solid-state microwave systems offer strong interactions for fast quantum logic and sensing but photons at telecom wavelength are the ideal choice for high-density low-loss quantum interconnects. A general-purpose interface that can make use of single photon effects requires < 1 input noise quanta, which has remained elusive due to either low efficiency or pump induced heating. Here we demonstrate coherent electro-optic modulation on nanosecond-timescales with only $0.16^{+0.02}_{-0.01}$ microwave input noise photons with a total bidirectional transduction efficiency of 8.7% (or up to 15% with $0.41^{+0.02}_{-0.02}$), as required for near-term heralded quantum network protocols. The use of short and high-power optical pump pulses also enables near-unity cooperativity of the electro-optic interaction leading to an internal pure conversion efficiency of up to 99.5%. Together with the low mode occupancy this provides evidence for electro-optic laser cooling and vacuum amplification as predicted a decade ago.

---

[1] Institute of Science and Technology Austria, am Campus 1, 3400 Klosterneuburg, Austria. ✉email: rsahu@ist.ac.at; jfink@ist.ac.at

Future quantum networks[1] between solid-state quantum systems[2] housed in separated cryogenic environments require efficient, low-noise, and high-bandwidth interfaces to telecom wavelength communication technology[3]. A general-purpose "quantum-enabled" interconnect must add $N_{\text{in}} < 1$ noise photons referenced to the input which allows for heralded quantum conversion and teleportation schemes in the presence of practical loss channels[4]. "Quantum limited" conversion with $N_{\text{in}} < 0.5$ and close to unity efficiency on the other hand will be required for fully deterministic protocols that also maintain the Wigner negativity of the input state[5,6]. On the practical side, high instantaneous bandwidth is important to be able to shape and match the temporal mode of itinerant microwave quantum states for high-fidelity deterministic quantum network protocols[7].

Growing efforts in a wide variety of systems[8–10] led to record device efficiencies close to 50%[11] using radiation pressure coupling, but the necessary noise properties could not be achieved with the so far reported N_{in} ranging from 3.2[11,12] to $\sim 10^4$[13,14]. Recent experiments have used short pump pulses with low duty cycle and cooperativity to reduce the average thermal load[15–17] culminating in a noise level of only 0.57 quanta referenced to a localized piezo-mechanical superconducting qubit excitation[16]. However, this does not circumvent the instantaneous effects such as destroying the qubit state and resonator degradation due to Cooper pair breaking[18], as well as difficult to control detunings of the optical cavity owing to the photo-refractive[19] or thermo-optic effects[20].

In contrast to such tightly integrated on-chip approaches based on superconducting thin films, in this work, the cavity mode volumes are chosen to be large. As a result, the Watt-scale powers of a pulse-shaped optical pump can be used without the aforementioned complications. This allows us to reach unity cooperativity and unlocks the fast and coherent time dynamics of a strongly interacting electro-optic system. Moreover, lowering the microwave mode occupancy for the same cooperativity we observe a transition from the classical to the quantum regime of multi-mode cavity quantum electro-optics[21].

Results

Physics and implementation. Electro-optic converters use the nonlinear properties of a non-centrosymmetric crystal to couple microwave and optical fields[21–23]. We enhance the nonlinearity using a high-quality cavity resonance for the optical and microwave fields[14,18,24–29]. A schematic of the experiment is shown in Fig. 1. The device, which was also used in ref. [14], consists of a lithium niobate whispering gallery mode optical resonator that is clamped by the metallic walls of a superconducting aluminum cavity. The latter is in situ tunable and designed to maximize the mode overlap between microwave and optical modes that respect the phase-matching condition, see Methods for device parameters.

The interaction Hamiltonian is given as $\hat{H}_{\text{int}} = \hbar g_0 (\hat{a}_e\hat{a}_p\hat{a}_o^\dagger + \hat{a}_e^\dagger\hat{a}_p\hat{a}_s^\dagger) + \text{h.c.}$, where, g_0 is the vacuum coupling rate and $\hat{a}_p$, and $\hat{a}_e$ represents the optical pump mode and microwave mode annihilation operators, respectively. $\hat{a}_o$ (optical signal mode), and $\hat{a}_s$ (Stokes mode) represents the optical mode annihilation operators on the blue and red sides of the optical pump, respectively. The first term in the Hamiltonian is the beam splitter interaction between modes $\hat{a}_e$ and $\hat{a}_o$ with the anti-Stokes scattering rate Γ_{AS}. The second term corresponds to the two-mode squeezing between modes $\hat{a}_e$ and $\hat{a}_s$ with the Stokes scattering rate Γ_S. We suppress phase-insensitive amplification owing to Γ_S via cross-polarization coupling of the Stokes mode $\hat{a}_s$ with a polarization-orthogonal degenerate optical mode, $\hat{a}_r$[25,30]. This hybridizes the optical mode $\hat{a}_s$ limiting its participation in the dynamics, as schematically shown in the optical spectrum in Fig. 1. The Hamiltonian is then given as

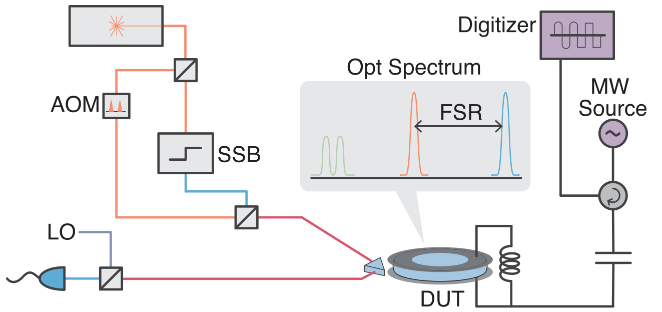

Fig. 1 Schematic of the experiment. The laser is divided into two parts: the optical pump and the signal. The pump is pulsed via an acousto-optic modulator (AOM). The signal part is frequency up-shifted using a single sideband modulator (SSB). The optical pump and signal are combined and sent to the device under test (DUT) in a dilution refrigerator via an optical fiber. The microwave signals are sent and received using a single port via a circulator. Optical and microwave output signals are measured with heterodyne detection.

$$\hat{H}_{\text{int}} = \hbar g_0(\hat{a}_e\hat{a}_p\hat{a}_o^\dagger + \hat{a}_e^\dagger\hat{a}_p\hat{a}_s^\dagger) + iJ\hat{a}_s^\dagger\hat{a}_r + \text{h.c.}, \qquad (1)$$

where J is the cross-polarization coupling rate between the $\hat{a}_s$ and $\hat{a}_r$ modes.

The figure of merit in electro-optic systems is the cooperativity $C = 4\bar{n}_p g_0^2/(\kappa_o\kappa_e)$, where $\bar{n}_p$ stands for the number of optical pump photons inside the optical resonator and κ_o (κ_e) for the total loss rate of the participating optical (microwave) mode. In analogy, we define the cooperativity for characterizing the mode coupling $C_J = 4J^2/(\kappa_s\kappa_r)$. On resonance, the total transduction efficiency including the gain due to amplification is calculated in terms of the two cooperativities as

$$\eta_{\text{tot}} = \eta_o\eta_e\Lambda^2 \frac{4C\left(1+C_J^{-1}\right)^2}{\left(1+C+C_J^{-1}\right)^2}, \qquad (2)$$

with the two-mode coupling efficiencies $\eta_i = \kappa_{i,\text{ex}}/\kappa_i$ with $i = e, o$ and the factor Λ accounting for optical coupling loss due to spatial mode-mismatch of the input beam. The gain due to amplification depends on the suppression ratio $\mathcal{S} = \Gamma_S/\Gamma_{AS} = (1 + C_J)^{-1}$. For $J \to \infty$, i.e., perfect suppression $\mathcal{S} = 0$, Eq. (2) reduces to the simple triply resonant model, as shown in the Supplementary Information, thus defining the (hypothetical) pure conversion efficiency without gain. We furthermore define the internal transduction coefficient by factoring out the measured coupling losses from the measured and calibrated total transduction efficiency, as $\eta_{\text{in}} = \eta_{\text{tot}}/(\eta_o\eta_e\Lambda^2)$.

High cooperativity pulsed conversion. Figure 2a, e shows the calibrated conversion efficiency for microwave-to-optics and optics-to-microwave conversion, respectively, for different cooperativities. The converted pulses are measured for two cases with a 200 MHz bandwidth, i.e., a CW signal (solid lines) and a pulsed signal while the pulsed optical pump pulse is on (dashed lines). The solid and dashed lines show the theoretical prediction from the numerical model with the input optical loss as the only fit parameter. We generally find excellent agreement and assign the observed mismatch in Fig. 2a for the case of pulsed signals to a small amount of uncorrected output filter drift.

We observe a large overshoot at the beginning of the converted pulse for CW signals (solid lines) and a smaller one for high cooperativity pulsed signals (dashed lines). The former appears because the cavity is pre-loaded with photons which get converted immediately when the optical pump pulse arrives. This momentarily

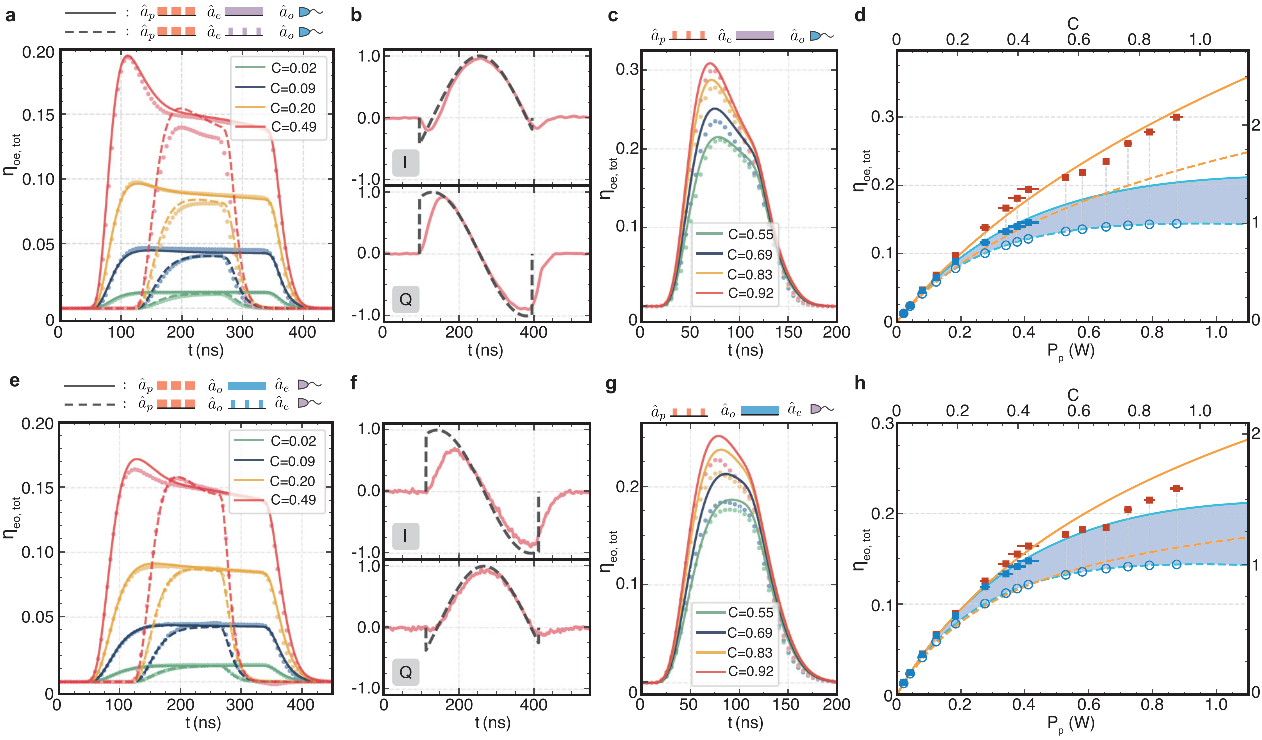

Fig. 2 High cooperativity bidirectional conversion. Top (bottom) row panels show results for microwave-to-optics (optics-to-microwave) conversion. **a**, **e** Converted signal pulses (bright dots are calibrated measurements and lines are theory) for a 300 ns-long optical pump pulse measured with a 500 Hz repetition rate for a CW signal (solid lines) and a pulsed signal (dashed lines). **b**, **f** Measured IQ quadrature modulation of the converted signal pulse (red lines) and the applied IQ quadrature modulation to the input signal (gray dashed lines) for $C = 0.49$. **c**, **g** Converted signal pulses (bright dots are calibrated measurements and lines are theory) for a 100 ns-long optical pump pulse and a CW signal measured with a 500 Hz repetition rate. **d**, **h** Summary of measured steady-state (blue squares) and peak (red squares) total transduction efficiency (left axis) and internal transduction coefficient (right axis) as a function of the in-pulse pump power P_p and cooperativity. Blue lines show the theoretical prediction for the steady-state (Eq. (2)) and orange lines for the peak values (see Supplementary Information), respectively. Solid lines are theory taking into account the finite suppression ratio $\mathcal{S} = 0.22$, whereas the dashed lines are for the ideal case $\mathcal{S} = 0$. The blue dashed line indicates the achieved C-dependent steady-state pure conversion efficiency and the blue-shaded area highlights the calculated gain of the measured steady-state transduction efficiency owing to finite sideband suppression. The vertical (smaller than the symbols) and horizontal error bars represent the standard error of the individual measured time-averaged values.

bypasses the coupling loss to the cavity and since $\eta_o \neq \eta_e$, the magnitude of this overshoot is different for the two directions of conversion. Importantly, there is also an overshoot in the case of pulsed signals (dashed lines) with $C \gtrsim 0.5$ because at high cooperativity the coherent interaction rate approaches that of the two-loss rates. This feature, therefore, represents the onset of coherent oscillations between microwave and optical photons in a strongly coupled electro-optic system.

For the measurement with $C = 0.49$, which corresponds to a parametrically enhanced coupling strength of $\sqrt{\bar{n}_p} g_0/(2\pi) = 6.58$ MHz with $\bar{n}_p = 3.16\times 10^{10}$ pump photons for a pulse pump power of $P_p \approx 0.4$ W, we explicitly show real-time complex quadrature control in Fig. 2b, f, as required for high-fidelity quantum communication protocols. A linear phase change is imprinted on the input signal pulses while keeping the amplitude constant. The measurements of the two converted quadratures match the input modulation closely. The only exception is during the beginning and the end of the optical pump pulse owing to the finite transducer bandwidth of 18 MHz for this C.

In order to reach $C \approx 1$, without entering an observed regime of instability, we use shorter, i.e., 100 ns-long optical pump pulses as shown in Fig. 2c, g. The highest microwave-to-optical conversion efficiency momentarily reaches up to 30% for a CW signal tone. In very good agreement with theory, this is a result of three effects, i.e., the pre-loading of the microwave cavity, the increased gain for higher C, and the strong and coherent electro-optic interaction, which would reveal an oscillatory behavior if longer pulses could be sustained. The observed deviations from theory in Fig. 2g are caused by the slight broadening of the microwave mode linewidth owing to the increased average bath temperature, in agreement with CW pump experiments[14], an effect which the theory model does not take into account. The Supplementary Information shows measurements up to $C = 1.2$ where the optical Kerr effect leads to instability and amplification for this particular pump pulse length.

A summary of the measured transduction efficiencies as a function of the applied optical pulse power P_p and corresponding cooperativity C is presented in Fig. 2d, h. The red and blue colors show measured peak and steady-state values, respectively. Solid lines are predicted transduction efficiencies for our experimental parameters corresponding to $\mathcal{S} = 0.22$, whereas dashed lines represent the case of perfect suppression $\mathcal{S} = 0$. The blue-shaded area thus represents the gain owing to the not fully suppressed Stokes process. For $C \gtrsim 0.35$, the achieved internal transduction coefficient η_{in}, which we define operationally by dividing the measured η_{tot} by the measured coupling losses, can exceed 1. This is owing to signal pre-loading into the cavity and coherent electro-optic oscillations in case of the extracted peak values (red symbols), as well as due to gain. This is explained in detail in the Supplementary Information.

The blue circles indicate the corresponding pure conversion efficiencies (without gain) for itinerant photons up to $C = 0.92$, reaching $\eta_{\mathrm{in}} = 0.995$ and $\eta_{\mathrm{tot}} = 0.144$. As pure conversion

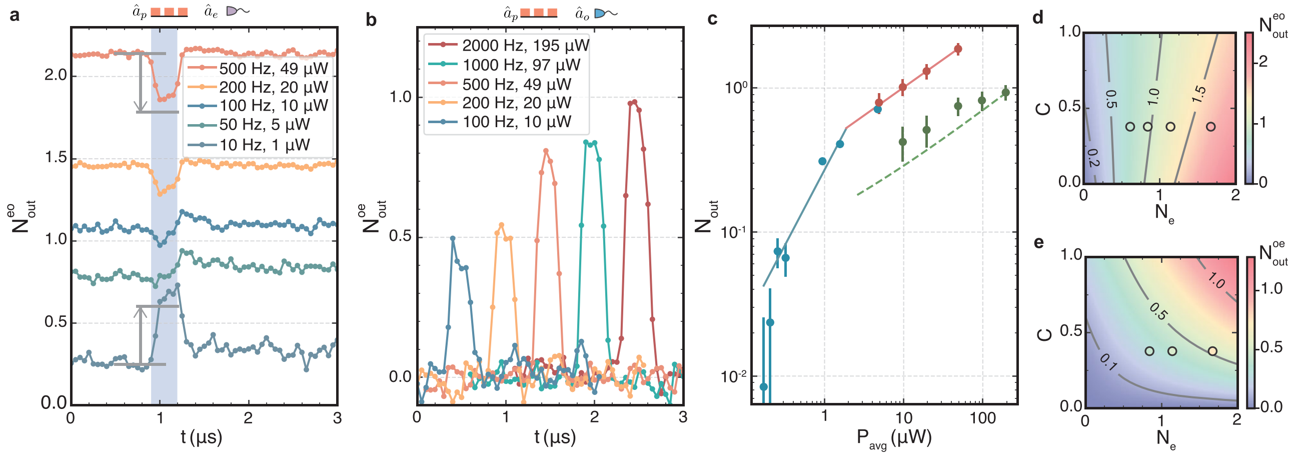

Fig. 3 Measured added noise during conversion. **a** N_{out}^{e} for a 300 ns-long optical pump pulse ($C = 0.38$) for different repetition rates f_{rep} (P_{avg}) measured with a 10 MHz bandwidth centered at the microwave resonance. The blue-shaded region shows the time span when the optical pump is on. The gray arrows mark the noise change as predicted from theory. **b** N_{out}^{o} for the same optical pump pulses and various f_{rep} (P_{avg}) measured with a 10 MHz bandwidth centered at the optical signal frequency. The noise pulses are separated in time for better visibility. **c** Compilation of all measured N_{out} for different time-averaged optical pump powers P_{avg}. Red and blue points represent measured N_{out}^{e} with 10 MHz and 100 kHz bandwidths, respectively. Green points represent N_{out}^{o} measured with 10 MHz bandwidth. The solid lines represent power-law fits. The green dashed line shows the predicted N_{out}^{o} using the measured N_{out}^{e}. All the points are taken with $C = 0.38$ ($\eta_{tot} = 11.4\%$) except for the first three blue points which correspond to $C = 0.20$ ($\eta_{tot} = 8.0\%$), 0.24 ($\eta_{tot} = 9.1\%$), and 0.3 ($\eta_{tot} = 10.3\%$), respectively. The error bars are inferred as in ref. [14]. For low occupancies, the confidence interval is given by the systematic error due to the absolute drift of the measurement baseline of ± 0.02 photons. **d** Density plot of the calculated N_{out}^{e} (10 MHz bandwidth) as a function of C and N_e for $\mathcal{S} = 0.22$. The top four measurements of N_{out}^{e} for the same $\mathcal{S}$ taken from **a** are shown as circles with experimental values represented by the inside color. **e** Density plot of the calculated N_{out}^{o} (10 MHz bandwidth) as a function of C and N_e for $\mathcal{S} = 0.22$. The left-most three measurements from **b** are shown as circles where experimental values are represented by the inside color.

efficiency estimates are based on a simplified theory calculation, we decided to instead focus on the measured steady-state transduction values and take into account the finite gain when calculating the corresponding added conversion noise, as explained below. The measured higher efficiencies due to signal pre-loading on the other hand are relevant to be able to make a fair comparison with the performance of current[16] and future interfaces that produce the signal photons inside the cavity and thus circumvent the microwave coupling losses.

Thermal and quantum noise. Figure 3 captures the effect of the two relevant types of noise. The first is thermal noise due to optical pump absorption heating, which depends on the time-averaged optical power $P_{avg} = P_p t_p f_{rep}$ with the pulse length t_p and the repetition rate f_{rep}. The second contribution is amplified vacuum noise due to finite transducer gain, which depends on $\mathcal{S}$ and P_p. The shown output noise photon numbers are defined by integrating the noise emission spectrum $S_{ii,out}$ (see Supplementary Information) over the Gaussian measurement filter function χ as $N_{out}^{i} = \int_{-\infty}^{+\infty} \chi(\omega) S_{ii,out}(\omega) d\omega$.

Figure 3a shows the microwave noise output N_{out}^{e} in the time domain, measured with a 10 MHz filter bandwidth (100 ns time resolution) centered at the microwave resonance, when 300 ns-long optical pump pulses with $C = 0.38$ are applied (shaded region) with different repetition rates from 10 to 500 Hz. High repetition rates increase the measured average thermal output noise, which stays approximately constant during the measurement time of 3 μs. During the pulse, however, we observe either a classical or a quantum effect depending on the average thermal occupancy of the microwave mode. For higher mode temperature (red curve), parametric laser cooling of the microwave mode[21], owing to upconversion of noise to optics is dominant and in agreement with theory (gray arrow). But as the thermal noise is decreased for the same cooperativity, additional noise due to vacuum amplification overwhelms the parametric cooling effect. For the lowest occupancy curve with a 10 Hz repetition rate, the vacuum amplification is clearly observed during the pump pulse and is in good agreement with theory (gray arrow). This last curve is measured with a lower suppression $\mathcal{S} \approx 0.82$ (using a different set of optical modes with a different magnitude of avoided crossing) in order to enhance the effect for a better signal-to-noise ratio. We assign slight mismatches between the theoretical prediction and experiment to an expected small amount of thermal heating during the pulse.

The observation of parametric laser cooling implies the presence of noise at the output of the optical signal mode $\hat{a}_o$. N_{out}^{o} is measured with a 10 MHz bandwidth around the optical signal frequency and shown in Fig. 3b. The optical pump pulses are the same as in Fig. 3a with varying repetition rates. With higher P_{avg}, the thermal microwave mode occupancy increases, thus, increasing the output optical noise.

We summarize these results in Fig. 3c as a function of P_{avg}. The N_{out}^{i} during the pulse from Fig. 3a are shown as red points, and from Fig. 3b as green points, along with corresponding power-law fits (solid lines). The dashed green line represents the predicted optical noise based on theory and the fitted microwave noise. In addition, we show microwave noise measurements conducted with a 100 kHz bandwidth for a better signal-to-noise ratio at the lowest occupancies where the system is deep in its quantum ground state (blue points), in agreement with ref. [14]. Unlike the triggered 10 MHz measurements, the 100 kHz measurements run continuously to sample the maximum of the emission noise spectral density due to the average thermal noise from the triggered optical pump pulses, resulting in (depending on C) up to ≈ 20% higher noise photon number values compared to the high-bandwidth measurements and thus represent a worst-case scenario for bandwidth matched time-domain conversion experiments. We report these higher values for the lowest achieved added conversion noise photon numbers.

In Fig. 3d, e, we show the theoretical prediction of the N_{out}^{e} and N_{out}^{o}, respectively, as a function of the steady-state microwave mode occupancy N_e and cooperativity C for the relevant experimental case $\mathcal{S} = 0.22$. As a function of N_e, in Fig. 3d the contours change from left-leaning to right-leaning as the transition from quantum amplification to classical cooling occurs. The measurements from Fig. 3a are shown as circles where the inside color represents the experimentally measured value in excellent agreement with the theoretical prediction. Similarly, the predicted dependence of N^o_{out} is shown in Fig. 3e where we included the measurements from Fig. 3b with good agreement with theory. Low bandwidth measurements (blue points in Fig. 3c) do not contain time-domain information and were therefore not included. These results provide strong evidence that P_{avg} fully determines the thermal noise limitations of this device. We furthermore find that the dilution refrigerator baseplate temperature, which went up to at most 60 mK for the highest P_{avg}, follows the same curve as reported in ref. [14] for continuous optical pump fields. This observed agreement with P_{avg} is expected due to the short pump timescales and the relatively high heat capacity leading to slow thermalization. The large difference between mode temperature N_e and the relatively cold dilution refrigerator is also owing to finite thermalization between the dielectric cavity where the heat originates, the superconducting cavity walls, and the cold dilution refrigerator baseplate bath.

Low occupancies and high cooperativity are the preconditions for interesting cavity quantum electro-optics experiments in analogy to cavity optomechanics[21] as well as for quantum-limited conversion. Figure 4a shows the calculated quantum cooperativity $C_q = C/N_e$—a measure of the electro-optic state transfer rate compared to the thermal decoherence rate of the microwave mode[31]—for the measurements in Fig. 3c, where N_e is inferred from the measured N^e_{out}. The achieved large $C_q \gg 1$ are a result of the low mode occupancies and encourage further investigations in the direction of two-mode squeezing of hybrid microwave and optical field states[32].

The most relevant quantity that signifies quantum-enabled conversion is the resulting equivalent added noise photon number referenced to the input of the converter where a non-classical input signal would be applied $S_{\mathrm{out}}(\omega) = \eta_{\mathrm{tot}}(S_{\mathrm{in}}(\omega) + N_{\mathrm{in}})$. The two measured N^i_{out} include both thermal and quantum noise contributions and we calculate the resulting equivalent added input noise photon number with $N^{ij}_{\mathrm{in}} = N^i_{\mathrm{out}}/\eta_{\mathrm{tot}}$. Low values of N^{ij}_{in} therefore require simultaneously high efficiency and low output noise, which is achieved in this work.

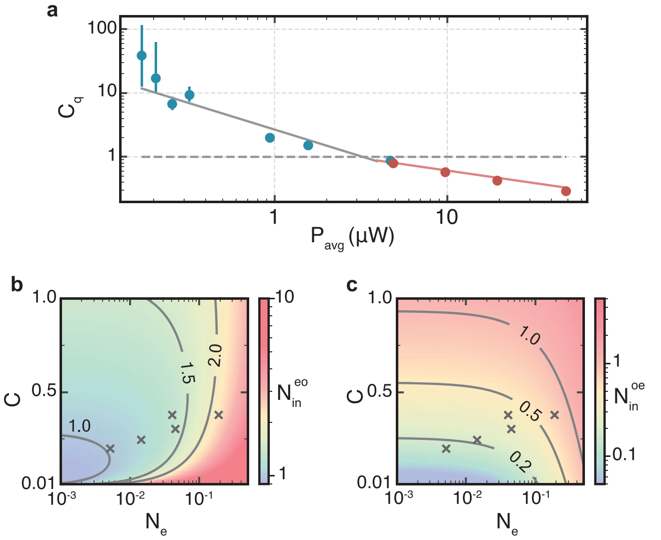

Fig. 4 Quantum cooperativity and equivalent input added noise. a Inferred quantum cooperativity $C_q = C/N_e$ for the measured output noise values shown in Fig. 3c. **b**, **c** Inferred optics-to-microwave N^{eo}_{in} (microwave-to-optics N^{oe}_{in}) equivalent added input noise as a function of C and N_e for $\mathcal{S} = 0.22$. Crosses mark the lowest five blue measurement points in Fig. 3c.

Figure 4b, d show N^{ij}_{in} for optics-to-microwave (N^{eo}_{in}) and microwave-to-optics (N^{oe}_{in}) conversion respectively as a function of N_e and C for $\mathcal{S} = 0.22$. The lowest five blue points from Fig. 3c are marked with crosses as the parameters we achieved experimentally. For N^{eo}_{in}, we reach $1.11^{+0.15}_{-0.07}$, and for N^{oe}_{in}, we reach as low as $0.16^{+0.02}_{-0.01}$ equivalent added noise photons. Here, the confidence interval is taken from error propagation using the confidence interval of the measured N^i_{out}.

Discussion

We have demonstrated a modular electro-optic transducer that converts itinerant photons from the microwave X to the telecom C band (and reverse) with a total bidirectional conversion efficiency of $\eta_{\mathrm{tot}} \approx 15\%$ (up to 30% for pre-loaded cavity states) with the demonstrated equivalent input noise $N^{oe}_{\mathrm{in}} < 1$ and a quantum cooperativity $C_q \gg 1$ for a cooperativity $C = 0.38$. Together with the phase-coherent control of the spectral and temporal dynamics with a bandwidth of up to 24 MHz, it is suitable for optically heralded superconducting quantum networking schemes[33] and the generation of non-classical correlations.

The new parameter regime of near-strong coupling cavity quantum electro-optics also enables the first systematic studies of dynamical and quantum back-action in electro-optic systems[21] as well as the deterministic generation of microwave-optics entanglement in the continuous variable domain[32]. This might lead the way for the scaling-up of error-protected superconducting quantum processor modules in large data centers but it could also find other applications such as for quantum-enhanced remote sensing[34] or sensitive radiometry[35], as well as for fiber-based classical control and readout of cryogenic qubit processors[36–38].

Current limitations include the somewhat complex assembly, the need for high pump powers, which leads to relatively slow pulse repetition rates, and the finite suppression ratio of the Stokes process, which is the dominant source of added noise at low average pump power. In future, these challenges can be addressed with more robust and compact packaging such as the proposed center-clamped design[32] that should also reduce phonon losses that might currently limit the microwave mode quality factor[39]. Such a thin-film approach would furthermore facilitate the use of thinner optical resonators with a larger electro-optic coupling that can help to avoid the optical instability owing to the Kerr effect.

Fabrication and material improvements have already led to optical quality factors that are 40 times higher than reported here. Maintaining this in a full device at low temperature would reduce the required pump power by three orders of magnitude for the same C, thus significantly reducing the thermal load and potentially allowing for much faster repetition rates. Narrower optical linewidths could also help to further improve the suppression of the Stokes process and the resulting amplified vacuum noise. Higher internal quality factors will furthermore be key to achieving higher external mode coupling ratios $\eta_{o,e}$ with the same bandwidth—a necessary requirement to push the total conversion efficiency for itinerant photons towards unity. This is needed for fully deterministic quantum interconnects operating in the quantum limit.

Methods

In this study, we use a device similar to ref. [14]. The optical WGMR is made from z-cut lithium niobate and enclosed in a machined aluminum cavity, which is designed to maximize the field overlaps and match the optical free spectral range

(FSR). The microwave mode is frequency tunable with internal linewidth $\kappa_{e,\mathrm{in}}/(2\pi) = 8.1$ MHz, coupling efficiency $\eta_e = 0.41$ and mode frequency $\omega_e/(2\pi) = 8.795$ GHz that accurately matches the optical FSR. The optical WGMR supports high-quality modes with an internal linewidth of $\kappa_{o,\mathrm{in}}/(2\pi) = 10.8$ MHz. The optical input and output are coupled to the WGMR mode via frustrated total internal reflection through an in situ movable diamond prism with $\Lambda \approx 0.78$ and $\eta_o = 0.58$ in this experiment. The optical mode $\hat{a}_r$ has a total linewidth of $\kappa_r/(2\pi) = 11.7$ MHz and is coupled to mode $\hat{a}_s$ with a coupling rate of $J/(2\pi) = 27$ MHz. These values are obtained from a comprehensive set of characterization measurements, which include phase-coherent time-domain 2 port scattering parameter measurements at $C \approx 1$ with an excellent agreement to theory, as reported in the Supplementary Information.

Data availability

All data sets and analysis files used in this study are available at https://doi.org/10.5281/zenodo.5984859.

Received: 27 October 2021; Accepted: 15 February 2022;
Published online: 11 March 2022

References

1. Wehner, S., Elkouss, D. & Hanson, R. Quantum internet: a vision for the road ahead. *Science* **362**, 303 (2018).
2. Clerk, A. A., Lehnert, K. W., Bertet, P., Petta, J. R. & Nakamura, Y. Hybrid quantum systems with circuit quantum electrodynamics. *Nat. Phys.* **16**, 257–267 (2020).
3. O'Brien, J. L., Furusawa, A. & Vučković, J. Photonic quantum technologies. *Nat. Photonics* **3**, 687–695 (2009).
4. Zeuthen, E., Schliesser, A., Sørensen, A. S. & Taylor, J. M. Figures of merit for quantum transducers. *Quantum Sci. Technol.* **5**, 034009 (2020).
5. Caves, C. M. Quantum limits on noise in linear amplifiers. *Phys. Rev. D.* **26**, 1817–1839 (1982).
6. Andrews, R. W., Reed, A. P., Cicak, K., Teufel, J. D. & Lehnert, K. W. Quantum-enabled temporal and spectral mode conversion of microwave signals. *Nat. Commun.* **6**, 10021 (2015).
7. Magnard, P. et al. Microwave quantum link between superconducting circuits housed in spatially separated cryogenic systems. *Phys. Rev. Lett.* **125**, 260502 (2020).
8. Lauk, N. et al. Perspectives on quantum transduction. *Quantum Sci. Technol.* **5**, 020501 (2020).
9. Lambert, N. J., Rueda, A., Sedlmeir, F. & Schwefel, H. G. L. Quantum information technologies: coherent conversion between microwave and optical photons - an overview of physical implementations. *Adv. Quantum Technol.* **3**, 2070011 (2020).
10. Han, X., Fu, W., Zou, C.-L., Jiang, L. & Tang, H. X. Microwave-optical quantum frequency conversion. *Optica* **8**, 1050–1064 (2021).
11. Higginbotham, A. P. et al. Harnessing electro-optic correlations in an efficient mechanical converter. *Nat. Phys.* **14**, 1038–1042 (2018).
12. Brubaker, B. M. et al. Optomechanical ground-state cooling in a continuous and efficient electro-optic transducer. *arXiv* https://arxiv.org/abs/2112.13429 (2021).
13. Arnold, G. et al. Converting microwave and telecom photons with a silicon photonic nanomechanical interface. *Nat. Commun.* **11**, 4460 (2020).
14. Hease, W. et al. Bidirectional electro-optic wavelength conversion in the quantum ground state. *PRX Quantum* **1**, 020315 (2020).
15. Forsch, M. et al. Microwave-to-optics conversion using a mechanical oscillator in its quantum ground state. *Nat. Phys.* **16**, 69–74 (2020).
16. Mirhosseini, M., Sipahigil, A., Kalaee, M. & Painter, O. Superconducting qubit to optical photon transduction. *Nature* **588**, 599–603 (2020).
17. Fu, W. et al. Cavity electro-optic circuit for microwave-to-optical conversion in the quantum ground state. *Phys. Rev. A* **103**, 053504 (2021).
18. Witmer, J. D. et al. A silicon organic hybrid platform for quantum microwave-to-optical transduction. *Quantum Sci. Technol.* **5**, 034004 (2020).
19. Jiang, H. et al. Fast response of photorefraction in lithium niobate microresonators. *Opt. Lett.* **42**, 3267–3270 (2017).
20. Jiang, W. et al. Lithium niobate piezo-optomechanical crystals. *Optica* **6**, 845 (2019).
21. Tsang, M. Cavity quantum electro-optics. *Phys. Rev. A* **81**, 063837 (2010).
22. Matsko, A. B., Strekalov, D. V. & Yu, N. Sensitivity of terahertz photonic receivers. *Phys. Rev. A* **77**, 043812 (2008).
23. Javerzac-Galy, C. et al. On-chip microwave-to-optical quantum coherent converter based on a superconducting resonator coupled to an electro-optic microresonator. *Phys. Rev. A* **94**, 053815 (2016).
24. Ilchenko, V. S., Savchenkov, A. A., Matsko, A. B. & Maleki, L. Whispering-gallery-mode electro-optic modulator and photonic microwave receiver. *J. Opt. Soc. Am. B* **20**, 333–342 (2003).
25. Rueda, A. et al. Efficient microwave to optical photon conversion: an electro-optical realization. *Optica* **3**, 597–604 (2016).
26. Fan, L. et al. Superconducting cavity electro-optics: a platform for coherent photon conversion between superconducting and photonic circuits. *Sci. Adv.* **4**, eaar4994 (2018).
27. Holzgrafe, J. et al. Cavity electro-optics in thin-film lithium niobate for efficient microwave-to-optical transduction. *Optica* **7**, 1714–1720 (2020).
28. McKenna, T. P. et al. Cryogenic microwave-to-optical conversion using a triply resonant lithium-niobate-on-sapphire transducer. *Optica* **7**, 1737–1745 (2020).
29. Xu, Y. et al. Bidirectional interconversion of microwave and light with thin-film lithium niobate. *Nat. Commun.* **12**, 4453 (2021).
30. Werner, C. S. et al. Control of mode anticrossings in whispering gallery microresonators. *Opt. express* **26**, 762–771 (2018).
31. Aspelmeyer, M., Kippenberg, T. J. & Marquardt, F. Cavity optomechanics. *Rev. Mod. Phys.* **86**, 1391 (2014).
32. Rueda, A., Hease, W., Barzanjeh, S. & Fink, J. M. Electro-optic entanglement source for microwave to telecom quantum state transfer. *npj Quantum Inf.* **5**, 1–11 (2019).
33. Krastanov, S. et al. Optically heralded entanglement of superconducting systems in quantum networks. *Phys. Rev. Lett.* **127**, 040503 (2021).
34. Barzanjeh, S. et al. Microwave quantum illumination. *Phys. Rev. Lett.* **114**, 080503 (2015).
35. Bagci, T. et al. Optical detection of radio waves through a nanomechanical transducer. *Nature* **507**, 81–85 (2014).
36. Lecocq, F. et al. Control and readout of a superconducting qubit using a photonic link. *Nature* **591**, 575–579 (2021).
37. Youssefi, A. et al. A cryogenic electro-optic interconnect for superconducting devices. *Nat. Electron.* **4**, 326–332 (2021).
38. Delaney, R. D. et al. Non-destructive optical readout of a superconducting qubit. *arXiv* https://arxiv.org/abs/2110.09539 (2021).
39. Goryachev, M., Kostylev, N. & Tobar, M. E. Single-photon level study of microwave properties of lithium niobate at millikelvin temperatures. *Phys. Rev. B* **92**, 060406 (2015).

Acknowledgements

The authors thank S. Wald and F. Diorico for their help with optical filtering, O. Hosten and M. Aspelmeyer for equipment, H.G.L. Schwefel for materials and discussions, L. Drmic and P. Zielinski for software support, and the MIBA workshop at IST Austria for machining the microwave cavity. This work was supported by the European Research Council under grant agreement no. 758053 (ERC StG QUNNECT) and the European Union's Horizon 2020 research and innovation program under grant agreement no. 899354 (FETopen SuperQuLAN). W.H. is the recipient of an ISTplus postdoctoral fellowship with funding from the European Union's Horizon 2020 research and innovation program under the Marie Skłodowska-Curie grant agreement no. 754411. G.A. is the recipient of a DOC fellowship of the Austrian Academy of Sciences at IST Austria. J.M.F. acknowledges support from the Austrian Science Fund (FWF) through BeyondC (F7105) and the European Union's Horizon 2020 research and innovation programs under grant agreement no. 862644 (FETopen QUARTET).

Author contributions

R.S., W.H., and A.R. worked on the setup and performed the measurements. R.S. did the data analysis. R.S., A.R., and L.Q. developed the theory. G.A. helped with the heterodyne calibration. R.S. and J.M.F. wrote the manuscript with contributions from all authors. J.M.F. supervised the project.

Competing interests

The authors declare no competing interests.

Additional information

Supplementary information The online version contains supplementary material available at https://doi.org/10.1038/s41467-022-28924-2.

Correspondence and requests for materials should be addressed to Rishabh Sahu or Johannes M. Fink.

Peer review information *Nature Communications* thanks Xu Han and the other anonymous reviewer(s) for their contribution to the peer review of this work. Peer reviewer reports are available.

Reprints and permission information is available at http://www.nature.com/reprints

Publisher's note Springer Nature remains neutral with regard to jurisdictional claims in published maps and institutional affiliations.

Open Access This article is licensed under a Creative Commons Attribution 4.0 International License, which permits use, sharing, adaptation, distribution and reproduction in any medium or format, as long as you give appropriate credit to the original author(s) and the source, provide a link to the Creative Commons license, and indicate if changes were made. The images or other third party material in this article are included in the article's Creative Commons license, unless indicated otherwise in a credit line to the material. If material is not included in the article's Creative Commons license and your intended use is not permitted by statutory regulation or exceeds the permitted use, you will need to obtain permission directly from the copyright holder. To view a copy of this license, visit http://creativecommons.org/licenses/by/4.0/.

© The Author(s) 2022